Article

Developing Quantitative Nondestructive Characterization of Nanomaterials: A Case Study on Sequential Infiltration Synthesis of Block Copolymers

Eleonora Cara,* Philipp Hönicke, Yves Kayser, Jörg K. N. Lindner, Micaela Castellino, Irdi Murataj, Samuele Porro, Angelo Angelini, Natascia De Leo, Candido Fabrizio Pirri, Burkhard Beckhoff, Luca Boarino, and Federico Ferrarese Lupi*

Read Online

ACCESS | Metrics & More | Article Recommendations | Supporting Information

ABSTRACT: The sequential infiltration synthesis (SIS) of inorganic materials in nanostructured block copolymer templates has rapidly progressed in the last few years to develop functional nanomaterials with controllable properties. To assist this rapid evolution, expanding the capabilities of nondestructive methods for quantitative characterization of the materials properties is required. In this paper, we characterize the SIS process on three model polymers with different infiltration profiles through *ex situ* quantification by reference-free grazing incidence X-ray fluorescence. More qualitative depth distribution results were validated by means of X-ray photoelectron spectroscopy and scanning transmission electron microscopy combined with energy-dispersive X-ray spectroscopy.
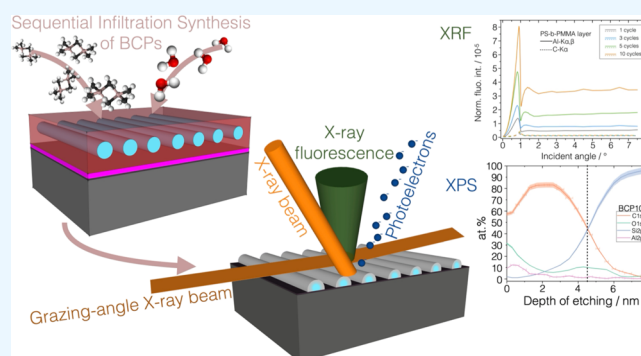
■ INTRODUCTION

Sequential infiltration synthesis (SIS), also known as vapor-phase infiltration, is a recently developed method for the synthesis of inorganic compounds inside polymeric materials. SIS is an extension of atomic layer deposition (ALD) where an ALD vapor-phase metal−organic precursor is dissolved inside the polymer, diffused toward the reactive functional groups, and entrapped in polymeric chains, where it forms a chemical bond and is converted to metallic oxide using a second coreactant precursor.[1,2] The chemical affinity of a wide variety of polymeric species and precursors has been tested, and a materials' library has been compiled in ref 3. The application of SIS to block copolymer (BCP) nanostructured templates results in the preferential growth of the metallic oxide in selected nanodomains.[4,5] Infiltrating inorganic compounds in polymers and BCP templates allows for the realization of nanomaterials with tailored functional properties yielding to several applicative fields. SIS opened up new possibilities for tuning the mechanical properties of the polymers, already quite versatile for pristine BCPs,[6] yielding increased etching resistance in pattern transfer processes,[7,8] increased Young modulus,[9] and swelled inorganic−organic BCP templates for an enhanced surface area for gas sensing.[10] Moreover, SIS constitutes a valid solution for tuning the polymer optical

constants for coatings,[11] for hyperbolic metamaterial engineering,[12,13] and for altering the polymers' electrical conductivity for nanoelectronics applications.[14] Interestingly, SIS has also been applied to the development of functional materials with scalable dimensions for applications including composite ultrafiltration membranes15,[16] and ceramic fibers for electrospinning.[17]

The exploitation of such advanced materials requires good control of the infiltration process and its mechanism through *in situ* analytical methods[18] as well as an accurate characterization of the outcome corresponding to the process parameters *ex situ* and of the resulting functional properties of the materials.[3,19] Among *in situ* analyses, Fourier-transform infrared (FTIR) spectroscopy has been used for monitoring the modifications of adsorption peaks corresponding to the interactions between polymers' functional groups and reactants,[20,21] allowing to propose a general mechanism that regulates trimethyl
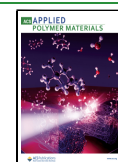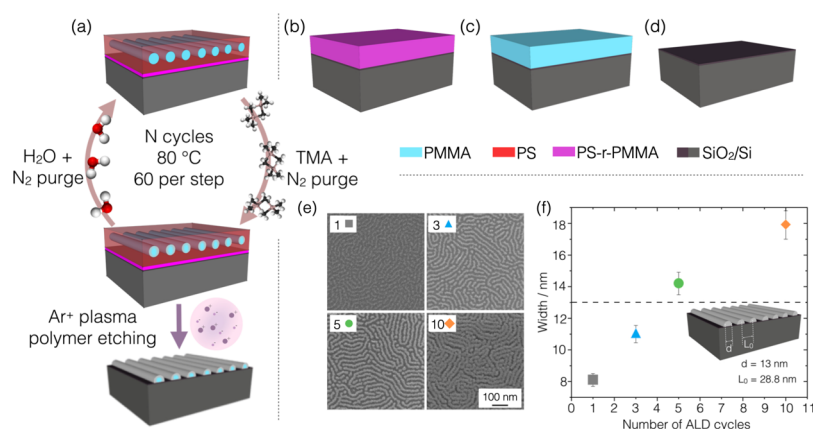
Figure 1. Schematic illustration of the four different samples treated under the same conditions by the ALD-based SIS process: (a) PS-*b*-PMMA layer with parallel cylinders of PMMA embedded in a PS matrix, (b) PS-*r*-PMMA layer, (c) high-M_w PMMA resist layer, and (d) bare Si/SiO$_2$ substrate. The color legend is reported on the right. Each type of sample was treated with N cycles of ALD using TMA and H$_2$O as vapor precursors to grow Al$_2$O$_3$, as schematized on the left-hand panel. Only for sample (a) the PS matrix was removed by argon plasma etching. (e) Resulting inorganic cylindrical domains are visible in the SEM images for a varying number of cycles reported in the top-left-corner boxes. (f) Scatter plot presents the lateral dimension of the cylindrical domains as a function of the number of ALD cycles, analyzed by two-dimensional Fourier transform on the corresponding SEM micrograph. The dashed line at 13 nm pinpoint the diameter d of pristine PMMA cylinders embedded in the PS matrix with center-to-center separation $L_0 = 28.8$ nm.

aluminum (TMA) infiltration in PS/PMMA-containing systems.[20] The chemical affinity of TMA with the carbonyl groups allows the selective growth of the organometallic precursor within the PMMA domains. Another recent FTIR study examined TMA and titanium tetrachloride (TiCl$_4$) precursors for alumina and titania, respectively, in polymethyl methacrylate (PMMA), poly(2-vinylpyridine) (P2VP), and polycaprolactone,[22] deeming them to be reactive to the chemical precursors. On the other hand, polystyrene was proved to be unreactive to such commonly used precursors, confirming previous results,[23] and thus used as a second block in BCPs, acting as a diffusion channel for the precursors for its large free volume and chemical incompatibility with the reactants.

An interesting characterization approach involved the multistep fabrication on delicate and expensive silicon nitride windows for the transmission electron microscopy (TEM) tomography of PS-*b*-PMMA nanodomains in directed self-assembly templates.[24] Complementary quartz crystal microbalance (QCM) gravimetry is often used for the determination of the inorganic compound's mass uptake inside the polymer.[25] However, an absolute quantification of the vapor-phase infiltration of the metallic oxide is still needed to improve the analytical capabilities on such composite materials.

Developing further methods for multidimensional and quantitative analysis is the aim of modern metrology for the characterization of advanced nanomaterials with special focus on the nondestructivity, absolute quantitative depth profiling at the nanoscale, traceability to the International System of Units (SI), and average analysis over extended area.[26] To achieve such a goal, the SIS in polymers offers an interesting case study for the characterization of composite nanomaterials which has indeed a dual importance. On the one side, better understanding the material's properties is essential to control the fabrication processes. On the other hand, such effort allows developing reference-free (RF) grazing incidence X-ray fluorescence (GIXRF) as a strong hybrid metrological tool, traceable to the SI, for the characterization of nanostructured materials with growing complexity. This paper presents the *ex*

situ characterization of the SIS process performed through RF-GIXRF on three different polymeric model systems, namely, self-assembled polystyrene-block-polymethyl methacrylate (PS-*b*-PMMA BCP, polystyrene-random-polymethyl methacrylate (PS-*r*-PMMA) random copolymer (RCP), and high-molecular-weight (M_w) PMMA resist. These model systems were purposely selected to obtain different infiltration profiles and were characterized for the cycle-dependent absolute quantification of the infiltrated inorganic compound. The GIXRF results were validated by characterizing the in-depth distribution of Al$_2$O$_3$ by X-ray photoelectron spectroscopy (XPS) and scanning transmission electron microscopy (STEM) combined with energy-dispersive X-ray spectroscopy (EDX).

■ RESULTS AND DISCUSSION

Sequential Infiltration Synthesis Processing. The polymeric model systems selected for the present study (PS-*b*-PMMA, P(S-*r*-MMA) and PMMA layers) are schematized in Figure 1a−c. On these model systems, SIS of alumina (Al$_2$O$_3$) was carried out by an ALD-based cyclic exposure to two vapor-phase reactants, TMA and water vapor, in single pulses alternated with nitrogen purges.[27] For each set of nominally identical samples, each one was treated with N = 1, 3, 5, or 10 ALD cycles together with a solid silicon substrate with a native oxide layer (Figure 1d) to parallelly monitor the deposition in a normal ALD process. The sample sets are labeled as BCP#, RCP#, PMMA#, and SUB# in the text, where the hash is substituted by the number of cycles. In Figure 1a, the SIS process is schematized for a BCP layer of PS-*b*-PMMA cylinders, oriented parallel to the substrate.

Among the sample sets, only the BCP samples were processed with argon plasma after the infiltration to remove the noninfiltrated matrix. The top-view scanning electron microscopy (SEM) micrographs (Figure 1e) reveal the Al$_2$O$_3$ replica of the fingerprint-like cylindrical nanodomains after 1, 3, 5, or 10 infiltration cycles, as reported in the top left box of each image. This is the first evidence that the infiltration occurred preferentially in the PMMA nanodomains as

described in ref 20, whereas the surrounding PS matrix was not infiltrated. The lateral size of the cylinders visibly increases with the number of cycles. A quantitative analysis of such an increment was performed on the SEM images by two-dimensional Fourier transform and radial averaging, and the values obtained are presented in Figure 1f as a function of the number of cycles. The dashed line in the graph marks the diameter of the pristine PMMA domains at 13 nm, while the scatter plot shows that in the first cycle the lateral size of the cylinder is reduced to (8.1 ± 0.4) nm. This indicates a reduction from the initial size and is ascribable to a subsurface infiltration of Al_2O_3 resulting in a smaller replica of the original cylinders. With an increasing number of cycles, the width of the inorganic nanostructures increases monotonically revealing an incremental uptake of the aluminum compound, externally to the first buried alumina layer, up to a width of (18 ± 1) nm at 10 cycles. The center-to-center pitch (L_0) of the cylinders remains equal to its initial value of 28.8 nm.

***Ex Situ* Quantitative GIXRF Characterization.** The four sample sets, as-infiltrated polymeric layers and SIS-processed BCP templates after PS removal (Figure 1e), were characterized using synchrotron radiation-based X-ray fluorescence analysis in its RF variant[28,29] (Figure S1a). Using the deconvoluted fluorescence spectra (as in Figure S1b), XRF allowed for the nondestructive analysis of the elemental composition and the absolute quantification, traceable to the SI, of the mass of Al per unit area, the areal density expressed in ng/cm^2.[30,31] The XRF quantification measurements are carried out at BESSY II synchrotron facility by using physically calibrated X-ray spectrometry instrumentation so removing the need for a calibration standard[28] and through the fundamental parameters approach based on Sherman's equation,[32] as reported in eq 1.

$$\sigma_e = \frac{N}{\epsilon(E_{e,K})} \cdot \frac{P_{e,K}}{\Phi_0} \cdot \frac{1}{\omega_{e,K} \cdot \tau_{e,K}(E_0)} \qquad (1)$$

The areal density of the element e, σ_e, was calculated by normalizing the fluorescence photon count rate of the corresponding fluorescence line of interest to the incident photon flux Φ_0 and the efficiency ε of the calibrated detector at the energy of the fluorescence peak and correcting for the factor N reported in the Experimental Section, eq 2. The last factor includes the atomic fundamental parameters involved in the fluorescence radiative decay at the K shell of the atom, i.e., the partial photoionization cross section τ at the energy of the incident beam and the fluorescence yield ω. The XRF measurements were performed in grazing incidence geometry where the angle of incidence was varied sequentially from 0° to far above the critical angle for total external reflection ($\theta_c \sim$ 1°). Using incidence angles below or in the vicinity of the critical angle of total external reflection allows reducing the contribution of the substrate to the fluorescence spectra increasing the detection sensitivity. Through GIXRF, the angular variation of the normalized fluorescence intensity of the element of interest allows to obtain information of its distribution either layer-like or bulk-like.[33] As an example, Al-Kα,β and Si-Ll angular profiles from sample SUB10 are reported in Figure 2a. The fluorescence intensities in the region well above the critical angle for total external reflection, on the right of the vertical dashed line shown in Figure 2a, present constant values independent of the angular variations. This region can be used for the quantification of the elemental
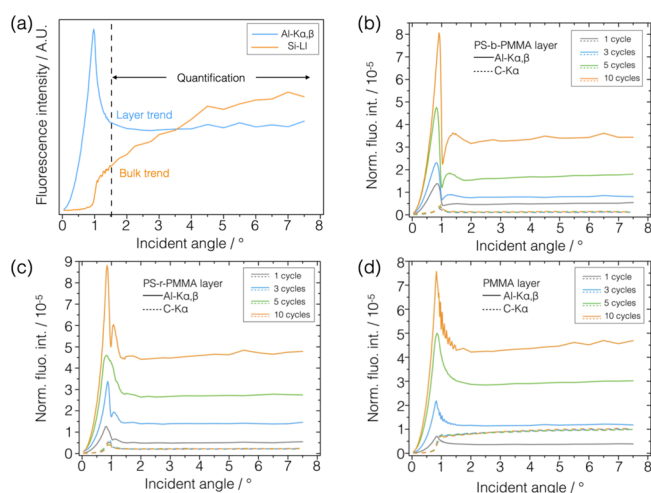

Figure 2. (a) Angular profile of the count rate for fluorescence lines Al-Kα,β and Si-Ll acquired on sample SUB10 exhibiting the layer-like trend and bulk-like trend, respectively, depending on the morphology of the sample and/or thickness of the elemental layer. The data in the angular range above the critical angle for total external reflection, above the vertical dashed line, can be used for the quantification of the element of interest. The normalized angular profile of the Al-Kα,β (solid line) and C-Kα (dashed line) fluorescence lines intensities are reported for the (b) PS-*b*-PMMA, (c) PS-*r*-PMMA, and (d) PMMA layers for different numbers of cycles. Carbon fluorescence angular profiles are more clearly visible in Figure S2 in the Supporting Information.

mass per unit area. The angular profile of the Al-Kα,β and C-Kα fluorescence line intensities is reported in Figure 2b−d with solid and dashed lines, respectively, for the three polymeric sample sets.

The carbon angular profiles at different ALD cycles exhibit a bulk-like trend in the PMMA samples (Figure 2d), indicating a thick slab of polymer, i.e., ~90 nm, while they have a layer-like trend in both PS-*r*-PMMA (Figure 2c) and PS-*b*-PMMA (Figure 2b) samples, i.e., thinner layers of ~30 and ~25 nm, respectively. By considering the carbon Kα fluorescence signal, the amount of carbon per unit area was calculated on the polymeric samples through eq 1. The graph in Figure 3a reports the relative mass per unit area, normalized to the value at the first cycle for each sample. This figure shows that the amount of carbon remains constant within the uncertainty in the PMMA and RCP samples infiltrated with different numbers of cycles. On the other hand, in the BCP samples treated with Ar plasma after SIS, the relative content of carbon is 30% higher in the BCP10 sample with respect to BCP1. This first result is ascribable to the increase in the lateral size observed in the SEM images in Figure 1e, where larger inorganic domains most likely inhibit the removal of the underlying random copolymer layer through plasma etching ending up with a higher relative mass content of carbon per unit area at 10 cycles.

Similarly, the average Al areal densities were calculated through eq 1 from the normalized fluorescence intensities (Figure 2b−d) of the aluminum Kα,β angular profiles presenting a layer-like trend in all three polymeric systems. In the angular range from 2.5 to 7°, suitable for quantification, the signal intensity increases with the number of cycles. The Al areal density as a function of the number of ALD cycles is reported in Figure 3b. The same XRF quantification measurements were repeated in different positions along 8−
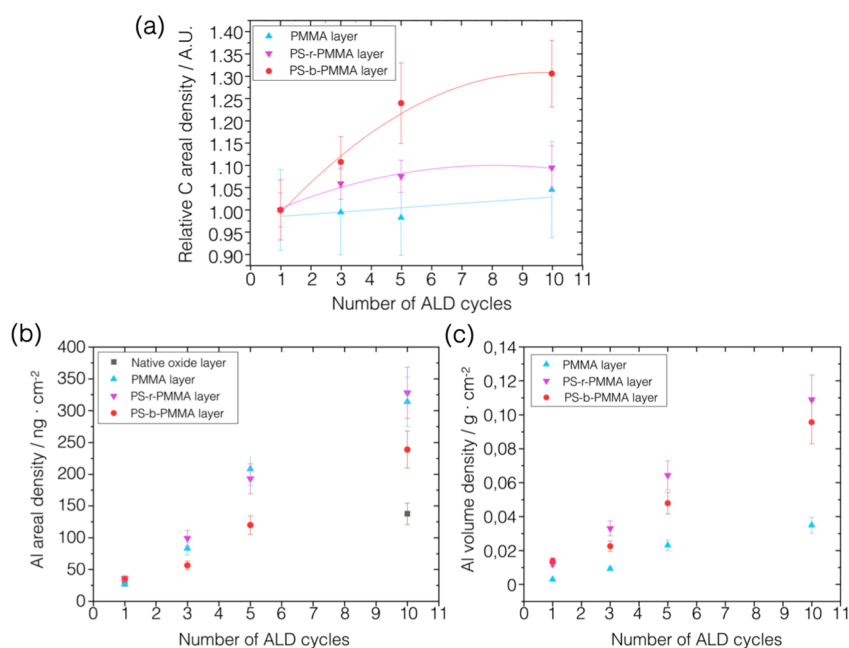
Figure 3. (a) Values of the carbon mass per unit area versus the number of ALD cycles are reported in the scatter plot normalized to the value at one cycle for the polymeric samples. (b) Values of the absolute areal density of Al for each sample set are reported as a function of the number of ALD cycles in the scatter plot. (c) Scatter plot of the aluminum mass per unit area normalized to the thickness of the polymeric layer measured prior to the infiltration process by spectroscopic ellipsometry.

10 mm to assess the homogeneity of the infiltration process across the sample. The results are reported in Figure S3 showing constant values within the error bars. Further details of the uncertainty evaluation are discussed in the Supporting Information.

The amount of deposited aluminum on the silicon wafers is (28 ± 4) ng/cm^2 in the first cycle (SUB1) and (138 ± 17) ng/cm^2 at 10 cycles (SUB10), corresponding to a layer thickness of 2.8 nm, and it gives a similar mass concentration within the uncertainties as compared to ALD processes performed on flat unpatterned substrates at the same temperature.[34] The polymeric samples can incorporate a much higher content of alumina increasing together with the number of cycles. The mass per unit area of aluminum increases from (27 ± 3) ng/cm^2 in PMMA1 to (314 ± 38) ng/cm^2 in the PMMA10 sample, while values of (328 ± 40) ng/cm^2 and (239 ± 29) ng/cm^2 were found in RCP10 and BCP10 samples, respectively. The larger content of aluminum inside RCP10 is ascribable to a higher fraction of PMMA (0.39) in RCP rather than in BCP samples (0.29) leading to a higher density of reactive sites.

To allow discussing the infiltration process in the different polymeric layers and comparing them, it should be taken into account that the polymers have different thicknesses, so in Figure 3c, the areal density data were normalized to the thickness of each polymeric layer. It was found that the most significant infiltration per unit volume occurred in the samples containing polystyrene, i.e., BCP and RCP samples, since PS facilitates the infiltration of the precursors and thus the formation of the alumina, consistently with the proposed mechanism for the infiltration of Al_2O_3 in PS/PMMA systems.[20] In addition, the GIXRF angular profiles acquired on the samples containing PS (Figure 2b,c) present a layer-like trend both for aluminum and carbon suggesting similar spatial elemental distributions for the inorganic and organic components. This observation is reasonably compatible with

a varying concentration of Al in the depth polymeric layers. In the RCP samples, the alumina is distributed randomly through the depth of the layer, since PMMA and PS chains do not have a regular arrangement. In the BCP samples, an inorganic component is distributed inside the organic PMMA cylinders replicating the fingerprint-like nanotemplates as shown in Figure 1f. As studied through the lateral size measurements of these inorganic replicas, during the first ALD cycle, the organometallic precursor diffused through the PS matrix toward and inside the low-M_w high-mobility PMMA nanocylinders, below their surface. After the removal of the PS matrix, the resulting inorganic domains replicate the pristine one but with a smaller lateral size. In the following cycles, the inorganic phase added up in the outer shell of the PMMA cylinders increases the lateral size of domains.

On the other hand, from Figure 3c, it was found that the PMMA samples incorporated the lowest amount of inorganic oxide with respect to their thickness. Most likely, the absence of polystyrene and the high-M_w polymeric chains with low mobility hindered the diffusion of the precursors. This is reflected in the GIXRF angular profiles (Figure 2d) where the carbon and aluminum fluorescence angular profiles exhibit bulk-like and layer-like trends, respectively, indicating two different distributions, likely a confined aluminum layer inside the polymer slab.

Validation by XPS, STEM, and EDX Characterization. In order to expand the nondestructive depth profiling capability of GIXRF, the results were validated by means of the analysis of the cross-sectional content of aluminum by *ex situ* layer-by-layer sputter etching and XPS analysis[35] performed on the as-fabricated samples. Additionally, thin electron-transparent cross-sectional lamellae of the infiltrated samples were prepared to perform the STEM imaging and the EDX chemical mapping. This combination of methods allows gaining information on the in-depth chemical constituent of the composite matrix while giving a direct visualization of the
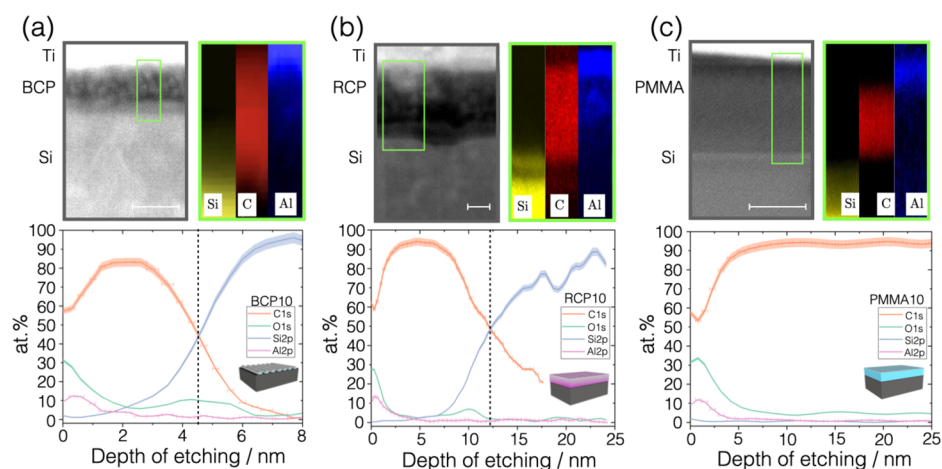
Figure 4. Depth profiles of (a) BCP10 PS-b-PMMA layer treated with 10 cycles, (b) RCP10, and (c) PMMA10 samples are displayed. In each column, from top to bottom, the schematic illustration of the infiltrated polymer is shown followed by the STEM micrograph of the region of interest. The scale bar is 5 nm in (a, b) and 50 nm in (c). EDX chemical maps are shown for silicon, carbon, and aluminum on the three samples. Finally, the elemental depth distribution, obtained from XPS spectra at each depth step, is reported in the depth range from 0 to 8 nm for sample BCP10 and from 0 to 25 nm for RCP10 and PMMA10, for the sake of comparison. The vertical dashed line marks the surface of the silicon substrate, although it is not visible in the depth profile (c) because the polymer is much thicker than 25 nm. The uncertainty on the depth of etching, reported as horizontal error bars in the Al2p and C1s curves, was obtained by standard propagation of the uncertainties δr and δc. Additional details and aluminum distribution curves from EDX and XPS data are presented in the Supporting Information.

region of interest. These analyses were performed on the polymeric samples treated with 10 ALD cycles assuming that the largest amount of infiltrated metallic oxide could guarantee good signal intensity and imaging contrast.[24] Figure 4a–c reports the results on the BCP10, RCP10, and PMMA10 samples, respectively. In the STEM images, titanium is visible on top of the sample, because this was used as a capping protective layer during the focused ion beam (FIB) preparation.

The STEM images referred to the PS-containing samples, BCP10 and RCP10 in Figure 4a,b, show the polymeric layer with a nebulous appearance due to the presence of infiltrated aluminum oxide. The EDX maps and the XPS profiles better clarify elemental distribution in the depth of the layer. For the sample BCP10 (Figure 4a), the concentration of aluminum is maximum near the polymer surface (Al 12.4 ± 0.1 atom %) and presents a gradient distribution toward the inner part of the polymeric domain with decreasing concentration, halved in the first 1 nm. The infiltration process leaves a thin mainly organic core or random copolymer buffer layer (visible in the schematics in Figure 1a). Both the XPS depth profile and STEM image reveal that the vertical size of the BCP domain is of the order of 5 nm, hence much smaller than the lateral size observed in top-view SEM analysis and of the thickness previous to SIS, due to the removal of the polymer matrix and collapse of the inorganic structures.[36] Similarly, a gradient-like decreasing trend of aluminum concentration is also observed inside the RCP10 carbon layer (Figure 4b) starting at 13.4 ± 0.2 atom % at the surface and decreasing monotonically in the first 5 nm of the layer, almost half of the organic layer thickness, reduced with respect to the pristine thickness consistently with ref 15. The information provided by GIXRF angular profiles is verified with what is observed in the chemical analysis along the z-axis. This revealed the presence of a top concentration of alumina and of a gradient distribution toward the center of the PS-containing polymeric domains and layer. The difference between the lateral size of the inorganic domains and their vertical size highlighted in the depth

profiling underlines the importance of combining hybrid analytical tools to characterize the same features of nanoscale composite materials.

As expected from the GIXRF analysis, a different trend was observed in the STEM micrograph of the PMMA10 sample (Figure 4c). This shows only a darker line in the top part of the polymeric layer ascribable to the inorganic infiltration. The same result is found in the EDX and XPS analyses showing an Al abundance concentrated in the first 4 nm, the top surface region of a thicker polymeric layer. Despite the presence of many reactive sites, the high molecular weight induces lower chain mobility and does not allow for an efficient channeling of the precursors in the depth of the polymer.

■ CONCLUSIONS

The presented inorganic replicas of block copolymers nano-domains are suitable candidates as reference materials for dimensional and analytical metrology at the nanoscale. They were already proposed as atomic force microscopy sub-20 nm lateral length standard[37,38] and they are candidate reference materials for hybrid chemical/dimensional nanometrology as they are being exploited in two different European projects (EMPIR 19ENV08 Aeromet II and 20FUN06 MEMQuD) as calibration standards. Ensuring the development of analytical methods for nondestructive and absolute quantification at the nanoscale is also essential to boost the applicability of complex organic–inorganic nanomaterials. RF GIXRF analysis is a well-established technique for the absolute quantification of the mass per unit area of deposited metals and other compounds.[29] The absolute quantification of infiltrated inorganics could be transferred to common mass uptake QCM gravimetric measurements used for in situ control of the SIS process. More effort is still needed to use solely the GIXRF angular curves, with appropriate modeling, to extract the in-depth characteristics of composite and inhomogeneous nanomaterials with varying densities and optical constants. The use of known polymer-precursor pairs, resulting in different infiltration profiles, served the scope of paving the way to expand its

depth profiling capabilities while using other destructive methods allowed validating the potential and application range of this method toward even more reliable nanometrology tools.

EXPERIMENTAL DETAILS

Preparation of the Polymeric Films. Silicon substrates with an ~1.6 nm native SiO_2 layer were used as a support for the deposition of the polymeric films. The 1 cm^2 substrates were cleaned by sonication in an acetone bath for 5 min and, consecutively, in an isopropanol bath for 2 min. The substrates' surface was then made hydrophilic by an O_2 plasma treatment (tabletop plasma cleaner *Plasma matrix Bdiscom*) performed at 100 W for 5 min. For the preparation of BCP self-assembled films, a layer of random copolymer (RCP) was prepared by spin coating at 3000 rpm for 30 s a solution with 18 mg of P(S-*r*-MMA) (styrene fraction of 0.62, M_n = 14.5 kg mol^{-1}) in 2 mL of toluene. The RCP was grafted on the SiO_2 surface by thermal annealing in an N_2 environment at 270 °C for 300 s, and excess ungrafted polymer was removed by sonication in isopropanol, as described previously.[39] Finally, BCP films were prepared from a solution of cylinder-forming PS-b-PMMA (styrene fraction of 0.71, M_n = 67 kg mol^{-1} and PDI = 1.09) purchased from Polymer Source Inc. and used without further purification. The BCP self-assembly process was promoted by annealing the samples at 260 °C for 120 s. The resulting layer was composed of PMMA cylindrical nanodomains with diameter d = 13 nm and center-to-center distance L_0 = 28.8 nm oriented parallel to the substrate and embedded in a PS matrix of ~25 nm in thickness. A scheme of the resulting PS-b-PMMA sample is shown in Figure 1a.

Two other polymeric sample systems were prepared by depositing polymeric solutions over the clean substrates by spin coating. Commercial PMMA resist for electron beam lithography (PMMA A4 M_n = 950 kg mol^{-1} *MicroChem*) was deposited at 3000 rpm for 60 s, obtaining a ~90 nm thick layer, schematized in Figure 1b. Random copolymer P(S-*r*-MMA), used as the grafting layer in the BCP self-assembly process, was simply spun under the same conditions, without any further treatment, to obtain an ~30 nm thick film.

SIS Procedure. The three polymeric sample systems were infiltrated with Al_2O_3. The SIS process was performed by ALD (*BENEQ TFS 200*) using TMA and H_2O as vapor precursors. The PS-b-PMMA, PMMA, and PS-r-PMMA polymeric samples were introduced in the ALD chamber together with a bare Si/SiO_2 substrate for reference. The four sample systems were treated by ALD with each cycle consisting of the injection of the TMA and a nitrogen purging step, followed by the injection of H_2O for the oxidation of aluminum and another N_2 purging step. Each step of the process was carried out at 80 °C for 30 s. All the samples were treated with N ALD cycles, either 1, 3, 5, or 10.

Morphological Characterization. To determine the morphology of the nanostructured BCP samples, the PS phase was removed after the SIS process exposing the fingerprint-like cylinders. The resulting morphology was characterized by field-emission gun scanning electron microscopy (FEG-SEM) (*FEI Inspect-F microscope*) in top-view configuration, as shown in Figure 1e, at an optimal working distance of 10 mm with magnification of 120,000×, with an electron acceleration voltage of 30 kV and a spot size of 3.5. The lateral size and center-to-center distance L_0 were determined at different cycles by processing the SEM micrographs, as reported in Figure 1f, by applying a two-dimensional Fourier transform and radial averaging analysis, already described in ref 40.

The thickness of the polymeric film was determined, on the pristine polymer after the spinning process, by spectroscopic ellipsometry measurements with an alpha-SE ellipsometer, J.A. Wollam Co. in the spectral range of 300−900 nm at a fixed angle of 70°, and the data were fit to a Cauchy model with CompleteEASE software.

GIXRF Measurements. The GIXRF measurements were conducted at the BESSY II synchrotron radiation facility. The beamline employed uses undulator radiation and is equipped with a plane grating monochromator (PGM)[41] such that soft X-rays with high spectral purity in the energy range from 78 to 1860 eV are provided. The low-divergence X-ray beam was characterized at the experimental end-station by a horizontal width of approximately 140 μm and a vertical width of 40 μm selected by an exit slit. An incident photon energy of 1622 eV was selected, well above the Al-K shell absorption edge (1559 eV) but still low enough to avoid the Si-Kα,β fluorescence emission originating from the bulk wafer material that would have reduced the detection limits of all elements. At the selected incident photon energy, only the resonant Raman scattering (RRS) produced in the Si wafer contributes with its continuous spectral distribution,[42] limiting the detection limits for elements having a spectral line close to the cut-off energy of the RRS spectrum. However, the grazing incidence conditions allow reducing the contribution from the substrate, i.e., bremsstrahlung radiation and RRS for the detection of aluminum. The beamline end-station is equipped with radiometrically calibrated instrumentation in an ultra-high vacuum (UHV) chamber with a 9-axis manipulator that allows for precise sample alignment in all degrees of freedom.[43] For the RF GIXRF measurements, the sample is rotated around one rotational axis labeled θ to vary the angle of incidence on the surface in the range from 0 to 7°. The fluorescence radiation is detected at 90° with respect to the primary beam direction, as schematized in Figure S1a, by means of a radiometrically calibrated silicon drift detector positioned at a well-defined distance from the sample. The incident photon flux I_0 is measured with absolutely calibrated photodiodes and the reflected photon flux photodiode characterized by a low dark current.

GIXRF Analysis. The recorded fluorescence spectra were individually deconvoluted to obtain the detector counts for each elemental line at every angle of incidence. The deconvolution process requires the knowledge on the detector response functions[44] for the fluorescence lines of interest and for the background contributions, e.g., the RRS at the Si-K edge and the bremsstrahlung radiation. A deconvoluted spectrum, excited at 4° on the PMMA10 sample, is reported in Figure S1b as an example. From the detector photon count rates $P_{Al,K}$ in eq 1, normalized count rates were obtained by multiplication to a normalization factor accounting for the incident θ-dependent solid angle of detection $\Omega/4\pi$, and a geometrical correction factor, as reported in eq 2.

$$N = \frac{\sin(\theta - \theta_0)}{\Omega/4\pi} \tag{2}$$

The detected count rates of the Al fluorescence lines in the angular range from 0° to about 2° are affected by the modulation of the XSW field and could provide information on the Al distribution. At larger incident angles, the reflected beam is negligible. Hence standard XRF excitation conditions are realized and the Al-Kα,β normalized count rate in this angular range provides information about the amount of infiltrated Al.

XPS Characterization. The XPS analysis was performed with a PHI 5000 Versaprobe Scanning X-ray Photoelectron Spectrometer (Physical Electronics, Chanhassen, MN, USA). An Al Kα X-ray source, at 15 kV voltage and 1 mA anode current, was used to provide monochromatic radiation at 1486.6 eV. All samples were attached to 2″ sample holder by means of double-sided conductive tape and were subject to a combined electron and Ar ion gun neutralizer system to decrease the electrical charging effect during the analysis. Working pressure, inside the main chamber, reached a maximum value of 10^{-6} Pa. The depth profiling was performed by the layer-by-layer etching of the composite samples through argon plasma generated at the same surface in a 2x2 mm^2 area. The XPS spectra were acquired in the center of the etched region after every etching time Δt. The time interval is chosen differently on different samples to be able to monitor the variation of the composition in depth. For BCP10 and RCP10 samples, Δt was selected to be 0.05 min (3 s), while for PMMA10 it was set at 0.1 min (6 s). The depth profiling was stopped when the Si2p signal was significantly higher than the C1s signal, indicating that the silicon substrate was reached. The atomic percent (atom %) of each species was found as a function of the time of

etching. The time of etching was then converted at each step to a depth of etching by multiplying the effective etch rate of the composite matrix to Δt. The effective etch rate was obtained by considering that etch rate varies progressively in the organic−inorganic mixture. A complete description of the XPS in-depth analysis is reported in the Supporting Information.

STEM and EDX Characterization. For the characterization by STEM, cross-sectional lamellae with a thickness of 30−40 nm were prepared from the samples treated with 10 ALD cycles by standard FIB micromachining and nanomanipulation, and the lamellae were mounted on a copper FIB grid (*Omniprobe*). The sample surface was protected from the FIB damage by means of a continuous layer of titanium (50 nm). On top of that, ion-beam induced deposition of platinum (1 μm thick) was used to cap the lamella during the etching procedures to preserve the region of interest in the thin polymeric layers. The STEM and concurrent EDX chemical analysis were performed with a cold field-emission gun transmission electron microscope (Cold FEG-TEM *Jeol NEOARM 200F*) at an acceleration voltage of 60 kV.

■ ASSOCIATED CONTENT

Ⓢ Supporting Information

The Supporting Information is available free of charge at https://pubs.acs.org/doi/10.1021/acsapm.2c02094.

> Additional experimental details are available concerning the GIXRF experimental setup, the results on carbon fluorescence angular profiles, the results on homogeneity of the infiltration process over large area, and the depth profiling by XPS and EDX. (PDF)

■ AUTHOR INFORMATION

Corresponding Authors

Eleonora Cara − *Advanced Materials and Life Science Division, Istituto Nazionale Ricerca Metrologica (INRiM), 10135 Torino, Italy;* ⓘ orcid.org/0000-0002-5981-9569; Email: e.cara@inrim.it

Federico Ferrarese Lupi − *Advanced Materials and Life Science Division, Istituto Nazionale Ricerca Metrologica (INRiM), 10135 Torino, Italy;* ⓘ orcid.org/0000-0002-1055-8839; Email: f.ferrareselupi@inrim.it

Authors

Philipp Hönicke − *Physikalisch-Technische Bundesanstalt (PTB), 10587 Berlin, Germany*

Yves Kayser − *Physikalisch-Technische Bundesanstalt (PTB), 10587 Berlin, Germany;* Present Address: Max Planck Institute for Chemical Energy Conversion, Stiftstr. 34-36, 45470 Mülheim an der Ruhr, Germany; ⓘ orcid.org/0000-0002-0301-2918

Jörg K. N. Lindner − *AG Nanostrukturierung, Nanoanalyse und Photonische Materialien, Paderborn University, 33098 Paderborn, Germany*

Micaela Castellino − *Dipartimento di Scienza Applicata e Tecnologia, Politecnico di Torino, 10129 Torino, Italy;* ⓘ orcid.org/0000-0002-1393-4043

Irdi Murataj − *Advanced Materials and Life Science Division, Istituto Nazionale Ricerca Metrologica (INRiM), 10135 Torino, Italy; Physikalisch-Technische Bundesanstalt (PTB), 10587 Berlin, Germany; AG Nanostrukturierung, Nanoanalyse und Photonische Materialien, Paderborn University, 33098 Paderborn, Germany; Dipartimento di Scienza Applicata e Tecnologia, Politecnico di Torino, 10129 Torino, Italy;* ⓘ orcid.org/0000-0001-9529-7959

Samuele Porro − *Dipartimento di Scienza Applicata e Tecnologia, Politecnico di Torino, 10129 Torino, Italy;* ⓘ orcid.org/0000-0003-3093-6099

Angelo Angelini − *Advanced Materials and Life Science Division, Istituto Nazionale Ricerca Metrologica (INRiM), 10135 Torino, Italy*

Natascia De Leo − *Advanced Materials and Life Science Division, Istituto Nazionale Ricerca Metrologica (INRiM), 10135 Torino, Italy;* ⓘ orcid.org/0000-0003-2154-1108

Candido Fabrizio Pirri − *Dipartimento di Scienza Applicata e Tecnologia, Politecnico di Torino, 10129 Torino, Italy*

Burkhard Beckhoff − *Physikalisch-Technische Bundesanstalt (PTB), 10587 Berlin, Germany*

Luca Boarino − *Advanced Materials and Life Science Division, Istituto Nazionale Ricerca Metrologica (INRiM), 10135 Torino, Italy;* ⓘ orcid.org/0000-0002-1221-2591

Complete contact information is available at:
https://pubs.acs.org/10.1021/acsapm.2c02094

Author Contributions

E.C. and F.F.L. conceptualized the idea. E.C., P.H., Y.K., M.C., S.P., F.F.L., I.M., and J.K.N.L. performed sample preparation, characterization, and data analysis. N.D.L., C.F.P., A.A., B.B., and L.B. provided funding and laboratory equipment. All authors contributed to writing and/or revising the manuscript.

Notes

The authors declare no competing financial interest.

■ ABBREVIATIONS

BCPs	block copolymers
PS-*b*-PMMA	polystyrene-*block*-polymethylmetacrylate
PS-r-PMMA	polystyrene-*random*-polymethylmetacrylate
SIS	sequential infiltration synthesis
GIXRF	grazing incidence X-ray fluorescence
ALD	atomic layer deposition
XPS	X-ray photoelectron spectroscopy
EDX	energy-dispersive X-ray spectroscopy
STEM	scanning transmission electron microscopy

■ REFERENCES

(1) Leng, C. Z.; Losego, M. D. Vapor phase infiltration (VPI) for transforming polymers into organic−inorganic hybrid materials: a critical review of current progress and future challenges. *Mater. Horiz.* **2017**, *4*, 747−771.

(2) Ingram, W. F.; Jur, J. S. Properties and applications of vapor infiltration into polymeric substrates. *JOM* **2019**, *71*, 238−245.

(3) Waldman, R. Z.; Mandia, D. J.; Yanguas-Gil, A.; Martinson, A. B.; Elam, J. W.; Darling, S. B. The chemical physics of sequential infiltration synthesis—A thermodynamic and kinetic perspective. *J. Chem. Phys.* **2019**, *151*, No. 190901.

(4) Peng, Q.; Tseng, Y. C.; Darling, S. B.; Elam, J. W. Nanoscopic patterned materials with tunable dimensions via atomic layer deposition on block copolymers. *Adv. Mater.* **2010**, *22*, 5129−5133.

(5) Kamcev, J.; Germack, D. S.; Nykypanchuk, D.; Grubbs, R. B.; Nam, C. Y.; Black, C. T. Chemically enhancing block copolymers for block-selective synthesis of self-assembled metal oxide nanostructures. *ACS Nano* **2013**, *7*, 339−346.

(6) Rana, D.; Mounach, H.; Halary, J. L.; Monnerie, L. Differences in mechanical behavior between alternating and random styrene-methyl methacrylate copolymers. *J. Mater. Sci.* **2005**, *40*, 943−953.

(7) Tseng, Y. C.; Peng, Q.; Ocola, L. E.; Elam, J. W.; Darling, S. B. Enhanced block copolymer lithography using sequential infiltration synthesis. *J. Phys. Chem. C* **2011**, *115*, 17725−17729.

(8) Cummins, C.; Ghoshal, T.; Holmes, J. D.; Morris, M. A. Strategies for inorganic incorporation using neat block copolymer thin films for etch mask function and nanotechnological application. *Adv. Mater.* **2016**, *28*, 5586−5618.

(9) Lorenzoni, M.; Evangelio, L.; Fernández-Regúlez, M.; Nicolet, C.; Navarro, C.; Pérez-Murano, F. Sequential infiltration of self-assembled block copolymers: A study by atomic force microscopy. *J. Phys. Chem. C* **2017**, *121*, 3078−3086.

(10) Pleshek, D.; Tran, J.; Li, Y.; Shirani, A.; Shevchenko, E. V.; Berman, D. Swelling-assisted sequential infiltration synthesis of nanoporous ZnO films with highly accessible pores and their sensing potential for ethanol. *ACS Appl. Mater. Interfaces* **2021**, *13*, 35941−35948.

(11) Berman, D.; Guha, S.; Lee, B.; Elam, J. W.; Darling, S. B.; Shevchenko, E. V. Sequential infiltration synthesis for the design of low refractive index surface coatings with controllable thickness. *ACS Nano* **2017**, *11*, 2521−2530.

(12) Murataj, I.; Channab, M.; Cara, E.; Pirri, C. F.; Boarino, L.; Angelini, A.; Ferrarese Lupi, F. Hyperbolic metamaterials via hierarchical block copolymer nanostructures. *Adv. Opt. Mater.* **2021**, *9*, No. 2001933.

(13) Alvarez-Fernandez, A.; Cummins, C.; Saba, M.; Steiner, U.; Fleury, G.; Ponsinet, V.; Guldin, S. Block copolymer directed metamaterials and metasurfaces for novel optical devices. *Adv. Opt. Mater.* **2021**, *9*, No. 2100175.

(14) Yu, Y.; Li, Z.; Wang, Y.; Gong, S.; Wang, X. Sequential infiltration synthesis of doped polymer films with tunable electrical properties for efficient triboelectric nanogenerator development. *Adv. Mater.* **2015**, *27*, 4938−4944.

(15) Waldman, R. Z.; Choudhury, D.; Mandia, D. J.; Elam, J. W.; Nealey, P. F.; Martinson, A. B.; Darling, S. B. Sequential infiltration synthesis of Al2O3 in polyethersulfone membranes. *JOM* **2019**, *71*, 212−223.

(16) McGuinness, E. K.; Zhang, F.; Ma, Y.; Lively, R. P.; Losego, M. D. Vapor phase infiltration of metal oxides into nanoporous polymers for organic solvent separation membranes. *Chem. Mater.* **2019**, *31*, 5509−5518.

(17) Azoulay, R.; Barzilay, M.; Weisbord, I.; Avrahami, R.; Zussman, E.; Segal-Peretz, T. Sequential Infiltration Synthesis for High-Precision Fabrication of Applied Ceramic Fibers with Designed Nanostructures− Nanowires, Nanobelts, and Core−Shell Fibers. *ACS Appl. Nano Mater.* **2022**, *5*, 7228.

(18) Cianci, E.; Nazzari, D.; Seguini, G.; Perego, M. Trimethyla-luminum diffusion in PMMA thin films during sequential infiltration synthesis: In situ dynamic spectroscopic ellipsometric investigation. *Adv. Mater. Interfaces* **2018**, *5*, No. 1801016.

(19) Cara, E.; Murataj, I.; Milano, G.; De Leo, N.; Boarino, L.; Ferrarese Lupi, F. Recent Advances in Sequential Infiltration Synthesis (SIS) of Block Copolymers (BCPs). *Nanomaterials* **2021**, *11*, 994.

(20) Biswas, M.; Libera, J. A.; Darling, S. B.; Elam, J. W. New insight into the mechanism of sequential infiltration synthesis from infrared spectroscopy. *Chem. Mater.* **2014**, *26*, 6135−6141.

(21) Biswas, M.; Libera, J. A.; Darling, S. B.; Elam, J. W. Kinetics for the sequential infiltration synthesis of alumina in poly (methyl

methacrylate): An infrared spectroscopic study. *J. Phys. Chem. C* **2015**, *119*, 14585−14592.

(22) Biswas, M.; Libera, J. A.; Darling, S. B.; Elam, J. W. Polycaprolactone: A Promising Addition to the Sequential Infiltration Synthesis Polymer Family Identified through In Situ Infrared Spectroscopy. *ACS Appl. Polym. Mater.* **2020**, *2*, 5501−5510.

(23) Peng, Q.; Tseng, Y. C.; Long, Y.; Mane, A. U.; DiDona, S.; Darling, S. B.; Elam, J. W. Effect of nanostructured domains in self-assembled block copolymer films on sequential infiltration synthesis. *Langmuir* **2017**, *33*, 13214−13223.

(24) Segal-Peretz, T.; Winterstein, J.; Doxastakis, M.; Ramírez-Hernández, A.; Biswas, M.; Ren, J.; Suh, H. S.; Darling, S. B.; Liddle, J. A.; Elam, J. W.; de Pablo, J. J.; Zaluzec, N. J.; Nealey, P. F. Characterizing the three-dimensional structure of block copolymers via sequential infiltration synthesis and scanning transmission electron tomography. *ACS Nano* **2015**, *9*, 5333−5347.

(25) Weisbord, I.; Shomrat, N.; Azoulay, R.; Kaushansky, A.; Segal-Peretz, T. Understanding and Controlling Polymer−Organometallic Precursor Interactions in Sequential Infiltration Synthesis. *Chem. Mater.* **2020**, *32*, 4499−4508.

(26) Orji, N. G.; Badaroglu, M.; Barnes, B. M.; Beitia, C.; Bunday, B. D.; Celano, U.; Kline, R. J.; Neisser, M.; Obeng, Y.; Vladar, A. E. Metrology for the next generation of semiconductor devices. *Nat. Electron.* **2018**, *1*, 532−547.

(27) Subramanian, A.; Doerk, G.; Kisslinger, K.; Daniel, H. Y.; Grubbs, R. B.; Nam, C. Y. Three-dimensional electroactive ZnO nanomesh directly derived from hierarchically self-assembled block copolymer thin films. *Nanoscale* **2019**, *11*, 9533−9546.

(28) Beckhoff, B. Reference-free X-ray spectrometry based on metrology using synchrotron radiation. *J. Anal. At. Spectrom.* **2008**, *23*, 845−853.

(29) Beckhoff, B. Traceable Characterization of Nanomaterials by X-ray Spectrometry Using Calibrated Instrumentation. *Nanomaterials* **2022**, *12*, 2255.

(30) Hönicke, P.; Kayser, Y.; Beckhoff, B.; Müller, M.; Dousse, J. C.; Hoszowska, J.; Nowak, S. H. Characterization of ultra-shallow aluminum implants in silicon by grazing incidence and grazing emission X-ray fluorescence spectroscopy. *J. Anal. At. Spectrom.* **2012**, *27*, 1432−1438.

(31) Müller, M.; Hönicke, P.; Detlefs, B.; Fleischmann, C. Characterization of high-k nanolayers by grazing incidence x-ray spectrometry. *Materials* **2014**, *7*, 3147−3159.

(32) Sherman, J. The theoretical derivation of fluorescent X-ray intensities from mixtures. *Spectrochim. Acta* **1955**, *7*, 283−306.

(33) Nowak, S. H.; Banaś, D.; Błchucki, W.; Cao, W.; Dousse, J. C.; Hönicke, P.; Hoszowska, J.; Kayser, Y.; Kubala-Kukuś, A.; Pajek, M.; Reinhardt, F. Grazing angle X-ray fluorescence from periodic structures on silicon and silica surfaces. *Spectrochim. Acta, Part B* **2014**, *98*, 65−75.

(34) Groner, M. D.; Fabreguette, F. H.; Elam, J. W.; George, S. M. Low-temperature Al2O3 atomic layer deposition. *Chem. Mater.* **2004**, *16*, 639−645.

(35) Sacco, A.; Bella, F.; De La Pierre, S.; Castellino, M.; Bianco, S.; Bongiovanni, R.; Pirri, C. F. Electrodes/electrolyte interfaces in the presence of a surface-modified photopolymer electrolyte: application in dye-sensitized solar cells. *ChemPhysChem* **2015**, *16*, 960−969.

(36) McGuinness, E. K.; Leng, C. Z.; Losego, M. D. Increased Chemical Stability of Vapor-Phase Infiltrated AlO x−Poly (methyl methacrylate) Hybrid Materials. *ACS Appl. Polym. Mater.* **2020**, *2*, 1335−1344.

(37) Aprile, G.; Ferrarese Lupi, F.; Fretto, M.; Enrico, E.; De Leo, N.; Boarino, L.; Volpe, F. G.; Seguini, G.; Sparnacci, K.; Gianotti, V.; Laus, M. Toward Lateral Length Standards at the Nanoscale Based on Diblock Copolymers. *ACS Appl. Mater. Interfaces* **2017**, *9*, 15685−15697.

(38) Dialameh, M.; Ferrarese Lupi, F.; Hönicke, P.; Kayser, Y.; Beckhoff, B.; Weimann, T.; Fleischmann, C.; Vandervorst, W.; Dubček, P.; Pivac, B.; Perego, M.; Seguini, G.; de Leo, N.; Boarino, L. Development and Synchrotron-Based Characterization of Al and

Cr Nanostructures as Potential Calibration Samples for 3D Analytical Techniques. *Phys. Status Solidi A* **2018**, *215*, No. 1700866.

(39) Sparnacci, K.; Antonioli, D.; Perego, M.; Giammaria, T. J.; Seguini, G.; Ferrarese Lupi, F.; Zuccheri, G.; Gianotti, V.; Laus, M. High temperature surface neutralization process with random copolymers for block copolymer self-assembly. *Polym. Int.* **2017**, *66*, 459−467.

(40) Ferrarese Lupi, F.; Murataj, I.; Celegato, F.; Angelini, A.; Frascella, F.; Chiarcos, R.; Antonioli, D.; Gianotti, V.; Tiberto, P.; Pirri, C. F.; Boarino, L.; Laus, M. Tailored and Guided Dewetting of Block Copolymer/Homopolymer Blends. *Macromolecules* **2020**, *53*, 7207−7217.

(41) Senf, F.; Flechsig, U.; Eggenstein, F.; Gudat, W.; Klein, R.; Rabus, H.; Ulm, G. A plane-grating monochromator beamline for the PTB undulators at BESSY II. *J. Synchrotron Radiat.* **1998**, *5*, 780−782.

(42) Müller, M.; Beckhoff, B.; Ulm, G.; Kanngießer, B. Absolute determination of cross sections for resonant Raman scattering on silicon. *Phys. Rev. A* **2006**, *74*, No. 012702.

(43) Lubeck, J.; Beckhoff, B.; Fliegauf, R.; Holfelder, I.; Hönicke, P.; Müller, M.; Pollakowski, B.; Reinhardt, F.; Weser, J. A novel instrument for quantitative nanoanalytics involving complementary X-ray methodologies. *Rev. Sci. Instrum.* **2013**, *84*, No. 045106.

(44) Scholze, F.; Procop, M. Modelling the response function of energy dispersive X-ray spectrometers with silicon detectors. *X-ray Spectrom.* **2009**, *38*, 312−321.